Science Bulletin 64 (2019) 36–43

Contents lists available at ScienceDirect

Science Bulletin

journal homepage: www.elsevier.com/locate/scib

Science Bulletin
www.scibull.com

Article

Efficient catalytic hydrogen generation by intermetallic platinum-lead nanostructures with highly tunable porous feature

Bin E [a,b], Lingzheng Bu [a], Qi Shao [a], Yujing Li [b,c], Xiaoqing Huang [a,*]

[a] College of Chemistry, Chemical Engineering and Materials Science, Soochow University, Suzhou 215123, China
[b] Department of Materials Science and Engineering, China University of Petroleum, Beijing 102249, China
[c] College of Materials, Beijing Institute of Technology, Beijing 100081, China

ARTICLE INFO

Article history:
Received 19 September 2018
Received in revised form 31 October 2018
Accepted 12 November 2018
Available online 30 November 2018

Keywords:
Porous
Selective etching
Hydrogen
Pt-Pb
Water-gas shift

ABSTRACT

The water-gas shift (WGS) reaction is an essential industrial reaction for upgrading hydrogen (H_2) by removing carbon monoxide (CO), while highly efficient platinum (Pt)-based catalysts for WGS with simultaneously high activity and stability are still yet to be developed due to the poisoning issue during the reaction. Herein, we report on the porous PtPb peanut nanocrystals (porous PtPb PNCs) and porous PtPb octahedron nanocrystals (porous PtPb ONCs) with controllable ratios of Pt/Pb as extremely active and stable catalysts towards WGS reaction. It exhibits the composition-dependent activity with porous PtPb PNCs-40/ZnO being the most active for WGS to H_2, 16.9 times higher than that of the commercial Pt/C. The porous PtPb PNCs-40/ZnO also display outstanding durability with barely activity decay and negligible structure and composition changes after ten successive reaction cycles. X-ray photoelectron spectroscopy (XPS) results reveal that the suitable binding energy of Pt $4f_{7/2}$ and the high ratio of Pt(0) to Pt(II) in porous PtPb PNCs/ZnO and porous PtPb ONCs/ZnO are crucial for the enhanced WGS activity. The CO stripping results indicate the optimized CO adsorption strength on the Pt surface ensure the excellent WGS activity and the outstanding durability. The present work demonstrates an important advance in tuning the porous metal nanomaterials as highly efficient and durable catalysts for catalysis, energy conversion and beyond.

1. Introduction

Water-gas shift (WGS) reaction is an important industrial reaction for upgrading hydrogen (H_2) in the fields of oil refining, ammonia synthesis and hydrogen fuel [1,2]. The main target of the WGS reaction is to remove the carbon monoxide (CO) formed during the upstream hydrocarbon reforming reaction to increase the H_2 yield as well as the H_2 purity. This step is essential since CO is often a poison for downstream processing catalysts, resulting in large activity decrease [3]. In industrial fields, the common systems contain a high temperature shift over Fe-Cr catalysts at 593–723 K and a low temperature shift over Cu-Zn-Al catalysts at 473–523 K [4]. However, these conventional systems are unsuitable for H_2 generation as required for fuel cell and other applications, because of their space-occupying, time-consuming, and poisoning-susceptibility [5,6]. Over the past decades, the researchers have noticed that platinum (Pt) group noble metals supported on reducible metal oxides, such as cerium oxide (CeO_2), titanium oxide (TiO_2) and zinc oxide (ZnO), which contain oxygen-vacancies, are more active for WGS [7–11]. Nonetheless, these Pt-based catalysts on reducible supports are not sufficiently stable and progressively deactivate due to the poisoning effect during the reaction [12]. Therefore, tremendous attentions have been focused on enhancing the anti-poisoning ability of Pt-based catalysts towards CO and thereby boosting the activity and durability for WGS.

Pt is extremely susceptible to the CO poisoning, which blocks the surface's active sites from further catalysis, thus resulting in dramatic efficiency decrease [13]. Therefore, weakening the strong CO adsorption may provide a useful way to improve the tolerance of the Pt-based catalysts towards CO poisoning [14]. In particular, alloying Pt with specific elements such as lead (Pb) exhibits high tolerance towards CO poisoning [15], providing an alternative way to enhance the anti-poisoning ability. Thanks to the geometric and electronic modifications, the Pt-Pt distance in Pt-Pb intermetallic compounds is distinct from that in other alloys or pure Pt. Such distance can mitigate the CO poisoning by reducing the

* Corresponding author.
E-mail address: hxq006@suda.edu.cn (X. Huang).

https://doi.org/10.1016/j.scib.2018.11.020
2095-9273/

bridge sites and eliminating the 3-fold hollow adsorption sites [13]. However, one thing should be noted that the introduction of excessive Pb may also decrease the WGS activity because of the weak CO adsorption. Therefore, seeking the best suitable CO adsorption on the surface of PtPb nanocrystals (NCs) and keeping the balance between the activity and the anti-poisoning ability is the essential point [16,17]. In fact, since the dependence of the charge distribution on the morphology and thus the different CO adsorptions on different shaped NCs, one reliable strategy for modulating the CO adsorption is to control their morphology [18]. However, realizing Pt-Pb catalysts with tunable morphologies is still a great challenge. Therefore, the development of efficient strategy to modulate the CO adsorption on the surface of PtPb NCs is highly desirable for enhancing the WGS catalysis.

Herein, for the first time we report a top-down strategy to create a new class of porous PtPb NCs (i.e., porous PtPb peanut NCs (porous PtPb PNCs) and porous PtPb octahedra (porous PtPb ONCs)), as highly efficient catalysts for WGS reaction. These porous PtPb PNCs with different porosities show promising activity to WGS reaction. In particular, the porous PtPb PNCs-40/ZnO with desirable porous degree exhibits excellent WGS activity with the outstanding turnover frequency value (TOF) of 3,730.6 h^{-1}, 1.3 and 16.9 times higher than the porous PtPb ONCs-40/ZnO (2,967.9 h^{-1}) and the commercial Pt/C (220.7 h^{-1}), respectively. The porous PtPb PNCs-40/ZnO also represents high stability with limited activity decay after ten cycles, due to the high anti-poisoning ability of Pb toward CO. X-ray photoelectron spectroscopy (XPS) results reveal that the porous PtPb PNCs-40/ZnO with the highest ratio of Pt(0) to Pt(II) shows the excellent WGS activity and the outstanding durability. Moreover, the CO stripping of porous PtPb PNCs-40/C shows that the relatively low onset and peak potentials for CO oxidation ensures suitable CO adsorption strength on the Pt surface for enhancing the WGS activity.

2. Materials and methods

2.1. Materials

Platinum(II) acetylacetonate ($Pt(acac)_2$, 97%), lead(II) acetylacetonate ($Pb(acac)_2$, 99%), *L*-ascorbic acid ($C_6H_8O_6$, AA, reagent grade, 99%), oleylamine ($C_{18}H_{37}N$, OAm, >70%), 1-octadecene ($C_{18}H_{36}$, ODE, technical grade, 90%), and Nafion (5%) were all purchased from Sigma-Aldrich (China). Glucose ($C_6H_{12}O_6$, analytical reagent), cyclohexane (C_6H_{12}, analytical reagent, >99.5%), ethanol (C_2H_6O, analytical reagent, >99.7%), perchloric acid ($HClO_4$, analytical reagent, 70%–72%) and nitric acid (HNO_3, analytical reagent, 65%–68%) were obtained from Sinopharm Chemical Reagent Co. (China). All the chemicals were used as received without further purification. The water (18 MΩ cm^{-1}) used in all experiments was prepared by passing through an ultra-pure purification system.

2.2. Synthesis of PtPb NCs and porous PtPb NCs

In a typical preparation of PtPb PNCs, 10.0 mg $Pt(acac)_2$, 8.0 mg $Pb(acac)_2$, 4.45 mg AA, 7.5 mg glucose, 2.5 mL OAm and 2.5 mL ODE were added into a glass vial (35 mL). After the vial had been capped, the mixture was ultrasonicated for 60 min. The resulting homogeneous mixture was then heated from room temperature to 160 °C in 30 min and maintained at 160 °C for 5 h in an oil bath, before it was cooled to room temperature. The resulting colloidal products were collected by centrifugation, and washed three times with an ethanol/cyclohexane mixture. All the synthetic parameters for PtPb ONCs are similar to those of PtPb PNCs but changing the reducing agent to *L*-ascorbic acid (17.8 mg). The porous PtPb PNCs were obtained by etching PtPb PNCs with nitric acid. In a typical preparation of porous PtPb PNCs, the PtPb PNCs were washed with ethanol/cyclohexane mixture for two times and then redispersed in cyclohexane (4.0 mL), oleylamine (0.5 mL) and 1-octadecene (0.5 mL). After being sonicated for several minutes, 1 mL nitric acid was added into the mixture. The mixture was then heated at desirable temperature for 1 h under stirring. To control the etching degrees of the porous PtPb PNCs, the temperature was changed from 30 to 40 and 60 °C. The preparation of porous PtPb ONCs was similar to that of porous PtPb PNCs except that the PtPb PNCs were replaced with PtPb ONCs.

2.3. Catalytic tests

The catalysts were fabricated by loading the PtPb PNCs, porous PtPb PNCs, PtPb ONCs and porous PtPb ONCs on the commercial carbon (C, Vulcan), aluminum oxide (Al_2O_3), zinc oxide (ZnO), cerium oxide (CeO_2) or titanium oxide (TiO_2) with 1% mass loading of Pt via simply sonicating the PtPb NCs and support in trichloromethane, then stirring for 3 h, and finally washing with ethanol. A 5 mg catalyst was used for each reaction. The water-gas shift reaction was performed in a 60 mL stainless-steel autoclave. After the addition of 10 mL H_2O and 5 mg catalyst into a Teflon inlet, the autoclave was pressurized with CO (1 MPa). The reaction was then performed at desirable temperature under stirring at 800 r/min. After the completion of the reaction, the gaseous mixture was analyzed using gas chromatograph (Agilent GC-7890B) equipped with a hayesep Q column connected to a thermal conductivity detector (TCD) and a 5 A molsieve column connected to a methane reformer with nickel catalyst and a flame ionization detector (FID). The yields of H_2 (Q_{H_2}) and the turnover frequency (TOF_{H_2}) based on the Pt are calculated using Eqs. (1) and (2).

$$Q_{H_2}\,(\mathrm{mmol}) = n_{H_2}\,(\mathrm{mmol}), \tag{1}$$

$$\begin{aligned}\mathrm{TOF}_{H_2}\left(\mathrm{h}^{-1}\right) &= n_{H_2}(\mathrm{mmol})/(n_{\mathrm{Pt}}(\mathrm{mmol}) \times t(\mathrm{h})) \\ &= n_{H_2}(\mathrm{mmol})/(m_{\mathrm{cat}}(\mathrm{g}) \times \mathrm{Pt}\ (\mathrm{wt\%}))/\left(M_{\mathrm{Pt}} \times 10^{-3}\left(\mathrm{g\ mmol}^{-1}\right)\right. \\ &\quad \left.\times\, t\ (\mathrm{h})\right),\end{aligned} \tag{2}$$

where, n is the amount of substance, m_{cat} is the quality of catalyst and M_{Pt} is molar mass of Pt.

2.4. Electrochemical measurements

A 2 mg carbon supported catalyst was ultrasonically dispersed in 0.4 mL isopropanol and 4 μL of 5% Nafion for 30 min. A 10 μL suspension was deposited on the precleared glassy carbon electrode and allowed to dry in air. A saturated calomel electrode (SCE) calibrated by a reversible hydrogen electrode (RHE) and a Pt wire were used as reference and counter electrodes, respectively. All the potentials were referred to RHE if not otherwise mentioned. The CO stripping experiments were tested at the rate of 20 mV s^{-1} at room temperature in 0.1 mol L^{-1} $HClO_4$ solution. The electrochemical surface area (ECSA) of the Pt in the working electrode is calculated using Eqs. (3) and (4). To calculate the per-site TOF, we used the Eqs. (5) and (6):

$$Q_{\text{co-adsorption}}\,(\mathrm{C}) = \int \frac{i\mathrm{d}E\,(\mathrm{mA\ V})}{v\,(\mathrm{mV\ s^{-1}})}, \tag{3}$$

$$\mathrm{ECSA}\,(\mathrm{m^2\ g^{-1}}) = \left[\frac{Q_{\text{co-adsorption}}\,(\mathrm{C})}{420\left(u\,\frac{\mathrm{C}}{\mathrm{cm^2}}\right) m_{\mathrm{Pt}}\,(\mathrm{mg})}\right], \tag{4}$$

$$\mathrm{TOF}_{\text{surface Pt}} = \frac{\text{Moles of reactant converted}}{\text{Active sites per real surface} \times \mathrm{ECSA} \times m_{\mathrm{Pt}} \times \text{reaction time}}, \tag{5}$$

$$\text{Active sites per real surface area} = \left(\frac{\text{Atoms per unit cell}}{v \text{ per unit cell}}\right)^{\frac{2}{3}}, \qquad (6)$$

where, v is the scanning speed, m_{Pt} is the mass of Pt.

2.5. Characterizations

The samples were prepared by dropping cyclohexane dispersion of samples onto the carbon-coated copper transmission electron microscopy (TEM) grids using pipettes and dried under ambient condition. Low-magnification TEM was conducted on a Hitachi HT7700 (Japan) transmission electron microscope at an acceleration voltage of 120 kV. High-magnification TEM was conducted on a FEI Tecnai F20 transmission electron microscope at an acceleration voltage of 200 kV. Energy dispersive X-ray spectroscopy (EDX) was performed on a scanning electron microscope (SEM, Hitachi, S-4700). Powder X-ray diffraction (PXRD) patterns were collected using an X'Pert-Pro X-ray powder diffractometer equipped with a Cu radiation source (λ = 0.15406 nm). The concentrations of catalysts were determined by the inductively coupled plasma-atomic emission spectrometer (ICP-AES) (Varian 710-ES, USA). XPS spectra were collected by XPS (Thermo Scientific, ESCALAB 250 XI, USA).

3. Results and discussion

3.1. Formation of PtPb NCs and porous PtPb NCs

The PtPb PNCs were produced through a solvothermal method by using platinum(II) acetylacetonate and lead(II) acetylacetonate as metal precursors, oleylamine and 1-octadecene as solvents and L-ascorbic acid and glucose as reducing agents. As revealed by TEM image, unique PtPb NCs with peanut-like structures were obtained. Fig. S1 (online) gives detailed morphological information of PtPb PNCs, where each NC consists of two domains with the length and diameter of (23.5 ± 1.0) nm and (11.6 ± 0.5) nm, respectively. The overall Pt/Pb composition was determined to be 50.7/49.3, in accordance with the Pt/Pb atomic ratio of the precursors, as confirmed by ICP-AES and SEM-EDX (Fig. S2a online). The PXRD shows that PtPb PNCs have typical intermetallic PtPb diffraction peak (JCPDS No. 06-0374) (Fig. S3a online).

Differ from the phase-segregation structure, the intermetallic PtPb PNCs offer new possibilities for fabricating porous PtPb PNCs by selectively removing the sacrificial component. Fig. 1a–d shows the schematic illustration of the resulted porous PtPb PNCs with different open structures via etching with nitric acid at different temperatures (see Section 2 for details), named porous PtPb PNCs-30, porous PtPb PNCs-40 and porous PtPb PNCs-60,

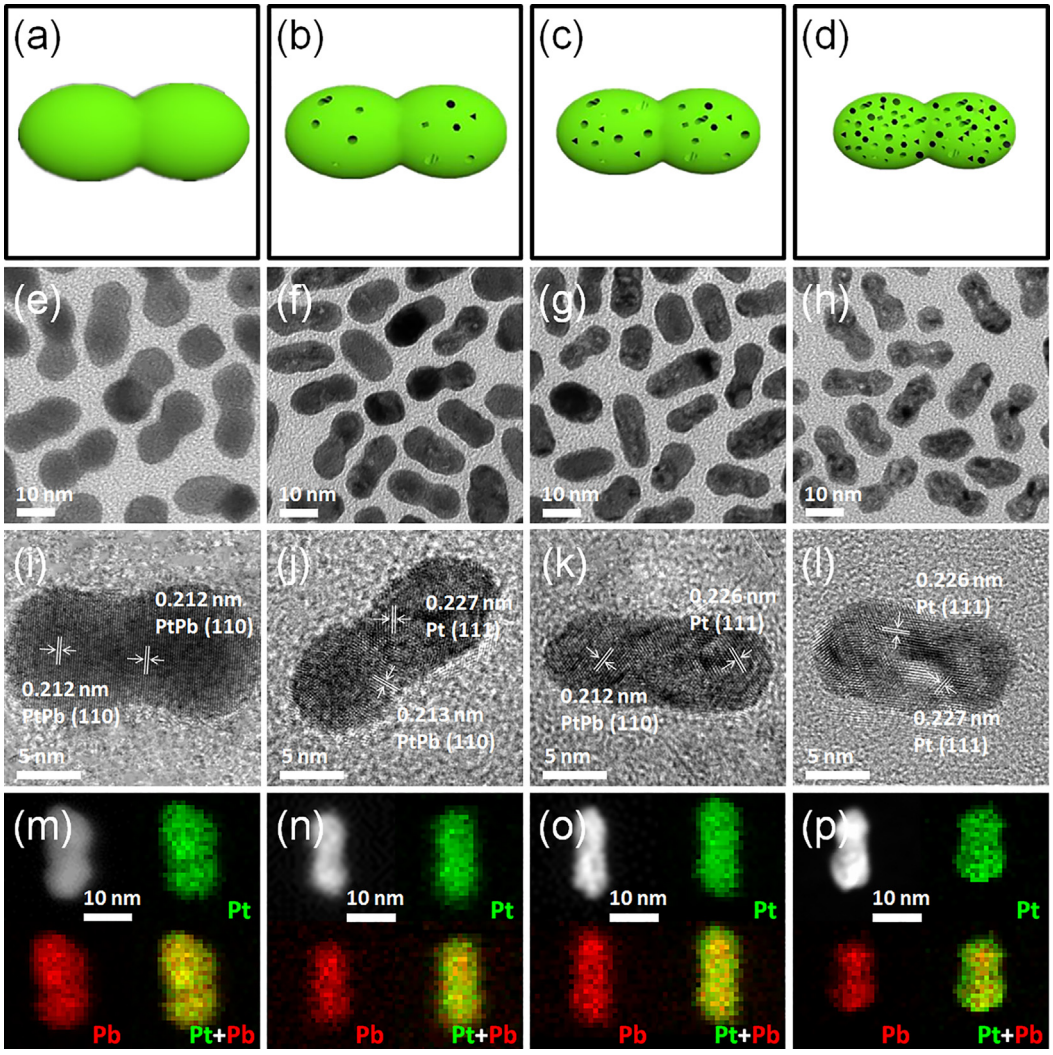

Fig. 1. (Color online) Morphological and structural characterizations of PtPb PNCs and porous PtPb PNCs. Schematic illustrations (a)–(d), TEM images (e)–(h), HRTEM images (i)–(l) and STEM-EDS elemental mappings (m)–(p) of PtPb PNCs (a, e, i, m), porous PtPb PNCs-30 (b, f, j, n), porous PtPb PNCs-40 (c, g, k, o) and porous PtPb PNCs-60 (d, h, l, p).

respectively. As shown in Fig. 1e–h, the profile of the PtPb NCs is largely maintained after the acid etching. More interesting, porous structures have been successfully created with the original peanut structure largely remained after etching at different temperatures. With the increase of the etching temperature, the length of porous PtPb PNCs decreases from (23.5 ± 1.0) to (17.5 ± 0.7) nm and the diameter decreases from (11.6 ± 0.5) to (8.2 ± 0.5) nm after the dissolution of Pb (Figs. S4–S6 online). The atomic ratios of Pt/Pb decreased from 50.7/49.3 (PtPb PNCs) to 64.7/35.3 (porous PtPb PNCs-30), 84.2/15.8 (porous PtPb PNCs-40) and 94.2/5.8 (porous PtPb PNCs-60) (Fig. S2 online). PXRD was used to illustrate the phase transformation from PtPb PNCs to the porous PtPb PNCs. The PtPb PNCs showed the typical intermetallic PtPb diffraction peaks. When etching by nitric acid at 30°, the porous PtPb PNCs-30 also showed the intermetallic PtPb phase while the peaks became boarder due to the small dissolution of Pb. With further increasing the etching temperature, complete phase changes were observed in the phases of the porous PtPb PNCs-40 and porous PtPb PNCs-60, where the pure Pt phase was observed (JCPDS No. 04-0802) (Fig. S3a online). The crystal phase of porous PtPb NCs gradually transfers from intermetallic PtPb phase to pure Pt phase (from (1 0 2) and (1 1 0) facets of PtPb phase to (1 1 1) facets of Pt phase) due to the Pb loss in etching process, which can be reflected by the shift around 40° of PXRD patterns in Fig. S3 (online). High-resolution TEM (HRTEM) was further carried out to reveal the porous structure and phase features (Fig. 1i–l). After nitric acid treatment, both lattice spacings of 0.212 and 0.227 nm were observed in porous PtPb PNCs-30 and porous PtPb PNCs-40, which are corresponding to the PtPb (1 1 0) plane and Pt (1 1 1) plane, respectively. However, only the lattice spacing of 0.227 nm, assigned to the (1 1 1) plane of Pt, was found in porous PtPb PNCs-60, in consistent with the PXRD result. The STEM-EDS elemental mappings of porous PtPb PNCs show that the Pt distributes throughout the entire NCs, while the Pb mainly distributes on the interior due to the dissolution of Pb (Fig. 1m–p). These results suggest that the abundant of Pb in the initial PtPb PNCs were etched away with the porosities largely depending on the etching temperatures. These porous PtPb PNCs with similar morphology but different Pt/Pb ratios provide a unique platform to explore the relationship between CO adsorption and Pt/Pb ratios.

Controlling the NCs shapes can also influence the CO adsorption on the surface of NCs by modulating the surface electronic properties of the catalysts [18]. Therefore, PtPb ONCs with the same Pt/Pb ratio yet different shapes were also successfully created, which were obtained by only using L-ascorbic acid (17.8 mg) as reducing agent (see Section 2 for details). The TEM images show that the products are dominated with octahedron morphology with the average length of 17.6 nm (Figs. 2a and S7 (online)). The SEM-EDX, PXRD, HRTEM and STEM-EDS elemental mappings results suggest the successful formation of octahedral

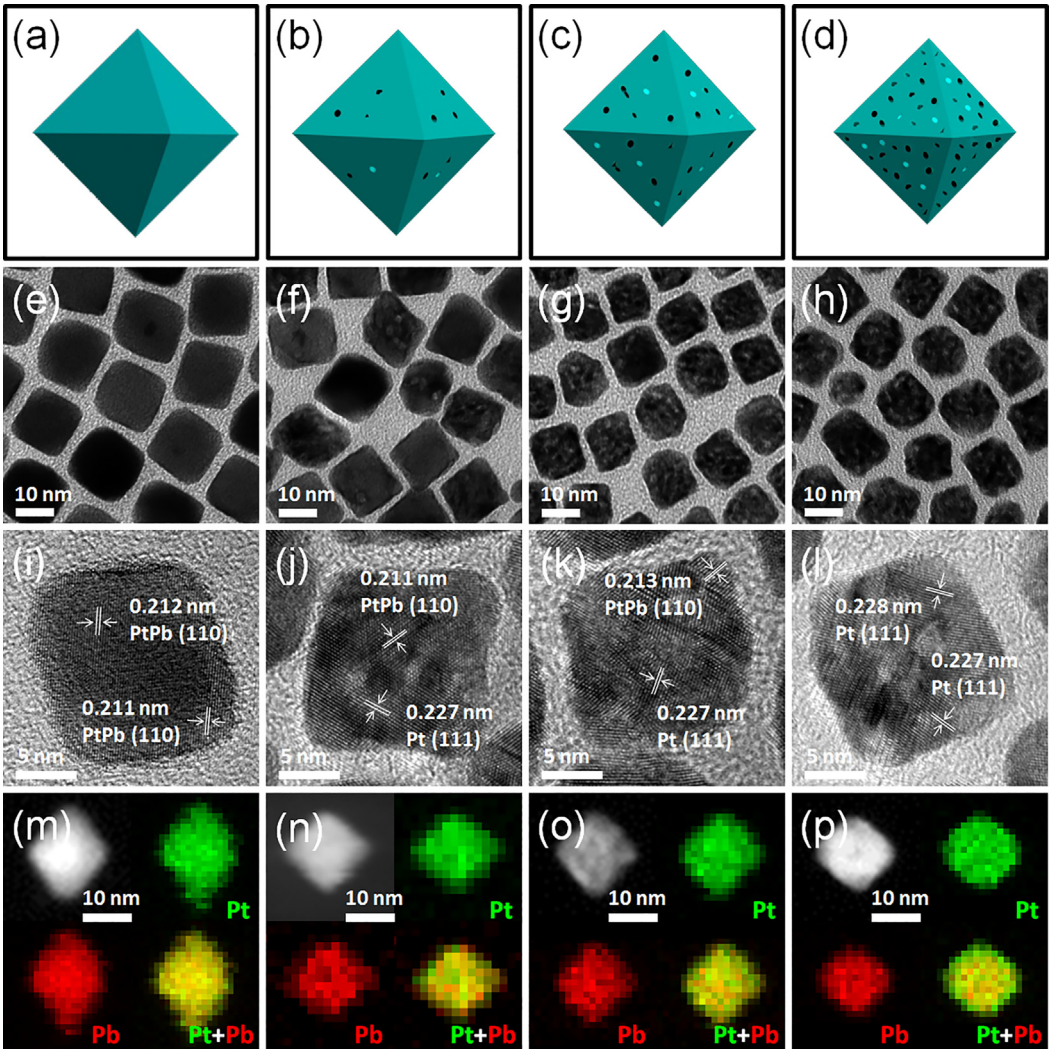

Fig. 2. (Color online) Morphological and structural characterizations of PtPb ONCs and porous PtPb ONCs. Schematic illustrations (a–d), TEM images (e–h), HRTEM images (i–l) and STEM-EDS elemental mappings (m–p) of PtPb ONCs (a, e, i, m), porous PtPb ONCs-30 (b, f, j, n), porous PtPb ONCs-40 (c, g, k, o) and porous PtPb ONCs-60 (d, h, l, p).

PtPb NCs. In a similar way, the PtPb ONCs were also subjected to chemical etching by nitric acid at different temperature to obtain the open structures with different porosity (Fig. 2b–d), named porous PtPb ONCs-30, porous PtPb ONCs-40 and porous PtPb ONCs-60, respectively. The higher acid treatment temperature accelerates the dissolution of Pb, which can be confirmed by the TEM images and SEM-EDX of porous PtPb ONCs, where the porous PtPb ONCs-60 shows the most obvious hollow structures with the length of (13.6 ± 0.5) nm and the lowest content of Pb of 4.5% (Figs. 2e–h and S8–S10 (online)). The structure transformation was illustrated by PXRD (Fig. S3b online). When etched by nitric acid, the PtPb ONCs has been converted from intermetallic PtPb into pure Pt phase, which is very similar to the case of PtPb PNCs. Fig. 2i–l shows the HRTEM images of PtPb ONCs, porous PtPb ONCs-30, porous PtPb ONCs-40 and porous PtPb ONCs-60. With the acid treatment, the lattice spacings of 0.227 nm assigned to the (1 1 1) plane of Pt appear in porous PtPb ONCs-30 and porous PtPb ONCs-40, while the lattice spacing of 0.212 nm assigned to the (1 1 0) plane of PtPb disappears in porous PtPb ONCs-60, further proving the complete formation to pure Pt phase. The STEM-EDS elemental mappings of porous PtPb ONCs (Fig. 2m–p) show the signal of Pb weakens with acid treatment, indicating the decrease of Pb and the formation of porous PtPb NCs.

3.2. WGS performances of PtPb NCs and porous PtPb NCs

The WGS reaction is an important industrial reaction for adjusting the H_2/CO ratios during the process of upstream hydrocarbon reforming to H_2 [1,2,19]. Here, the porous PtPb PNCs and porous PtPb ONCs with controllable Pt/Pb ratios provide a suitable platform to investigate the relationship between performance and Pt/Pb ratios. The performances of PtPb PNCs, porous PtPb PNCs, PtPb ONCs and porous PtPb ONCs for WGS were evaluated in details (Figs. 3 and 4). All the catalysts were fabricated by loading the catalysts on the commercial carbon or oxides (Figs. S11–S14 online). The effect from the molarity of K_2CO_3 on WGS was first explored since alkali ion-associated surface-OH groups are reactive toward CO in the presence of Pt, improving the efficiency in the WGS reaction [20–24]. The results show that, with the increased concentration of K_2CO_3, the activity of WGS enhances evidently and tends to be stable finally. The H_2 TOF can be maximized at 0.40 mol L^{-1} K_2CO_3 (2,249.5 h^{-1}) (Fig. 3a). Besides the molarity of K_2CO_3, the supports of reducible metal oxides, which contain oxygen-vacancies, are commonly used in WGS [25]. Among the five supports (C, TiO_2, ZnO, CeO_2 and Al_2O_3) examined, porous PtPb PNCs-60/ZnO exhibits the best performance (Fig. 3b). Therefore, ZnO is the best Supporting material for the porous PtPb PNCs-60, which is likely to due to the superior interfacial contact between

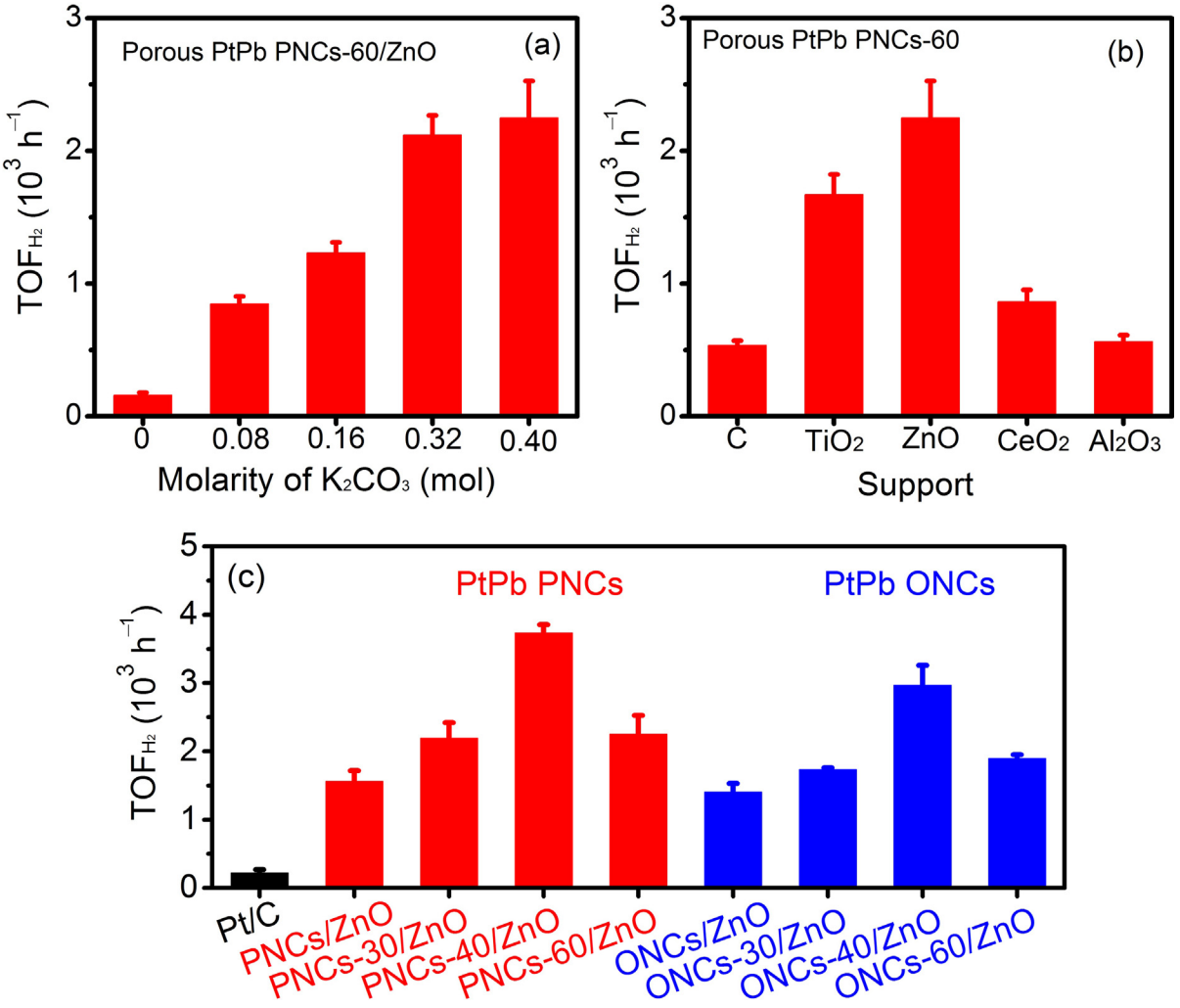

Fig. 3. (Color online) WGS of the PtPb PNCs, porous PtPb PNCs, PtPb ONCs, porous PtPb ONCs and commercial Pt/C. (a) The achieved H_2 TOF values of porous PtPb PNCs-60/ZnO with different molarity of K_2CO_3 at 200 °C for 1 h. (b) The achieved H_2 TOF values of porous PtPb PNCs-60 containing 0.40 mol L^{-1} K_2CO_3 with different supports at 200 °C for 1 h. (c) The achieved H_2 TOF values of the commercial Pt/C, PtPb PNCs/ZnO, porous PtPb PNCs/ZnO, PtPb ONCs/ZnO and porous PtPb ONCs/ZnO containing 0.40 mol L^{-1} K_2CO_3 at 200 °C for 1 h. Error bars correspond to the deviations from three-independent experiments.

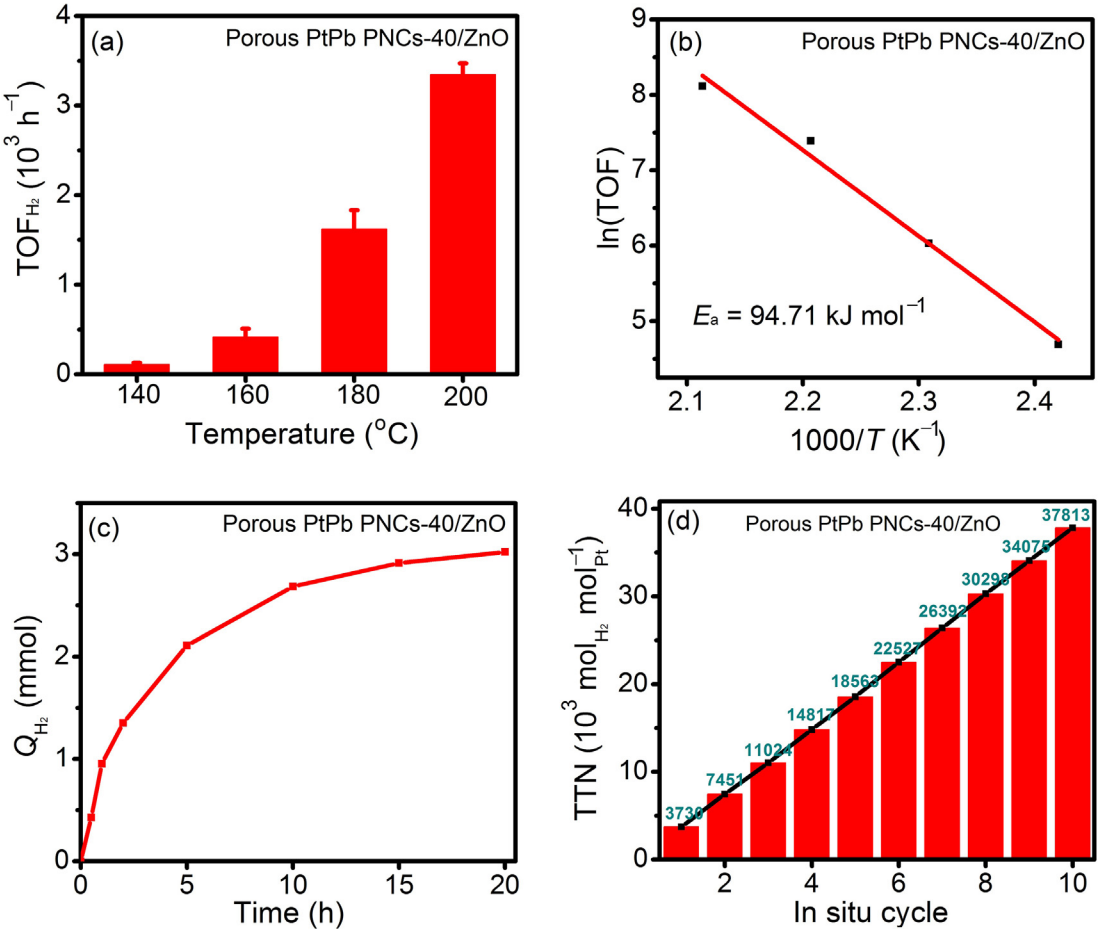

Fig. 4. (Color online) WGS of the porous PtPb PNCs-40/ZnO. (a) The achieved H_2 TOF values of porous PtPb PNCs-40/ZnO containing 0.40 mol L^{-1} K_2CO_3 at different reaction temperatures for 1 h. (b) The Arrhenius plot for the H_2 production of porous PtPb PNCs-40/ZnO. (c) The achieved H_2 production of porous PtPb PNCs-40/ZnO containing 0.40 mol L^{-1} K_2CO_3 at 200 °C for different reaction time. (d) The H_2 TTN values achieved by porous PtPb PNCs-40/ZnO over ten rounds of successive reactions.

Pt species and ZnO. In order to study the balance between the activity and the anti-poisoning ability, we started to seek the suitable Pt/Pb ratio to achieve the best suitable CO adsorption on the surface of PtPb NCs. As presented in Fig. 3c, the porous PtPb PNCs-40/ZnO shows the best performance for H_2 TOFs in all the investigated catalysts, much better than that of the commercial Pt/C (16.9 times). The porous PtPb PNCs-40/ZnO shows the TOF value of 3,730.6 h^{-1} for H_2, which is 2.4, 1.7 and 1.6 times higher than those of the PtPb PNCs/ZnO, porous PtPb PNCs-30/ZnO and porous PtPb PNCs-60/ZnO. Similarly, the typical volcano-like curves were also observed in porous PtPb ONCs/ZnO with the porous PtPb ONCs-40/ZnO showing the highest H_2 TOFs. In addition, the porous PtPb PNCs/ZnO achieved even better performance than the porous PtPb ONCs/ZnO with the H_2 TOF of porous PtPb PNCs-40/ZnO being 1.3 times higher than that of the porous PtPb ONCs-40/ZnO. Based on the above results, the porous PtPb PNCs-40/ZnO with the Pt/Pb ratio of 84.2/15.8 shows the best performance to H_2 in WGS reaction, even better than many Pt-based catalysts for WGS (Table S1 online).

Further detailed exploration of the performance of porous PtPb PNCs-40/ZnO was carried out in the following step. The H_2 TOF of WGS reaction increases with raising the temperature from 140 to 200 °C with porous PtPb PNCs-40/ZnO as catalyst (Fig. 4a). The associated apparent activation energy (E_a) value of porous PtPb PNCs-40/ZnO calculated by the arrhenius plot for H_2 production is 94.71 kJ mol^{-1} (Fig. 4b). The relatively low E_a value proves that porous PtPb PNCs-40/ZnO can effectively excite the CO molecule and thus high activity [26]. The catalytic behaviors of the porous PtPb PNCs-40/ZnO were further studied by exploring the H_2 yields as a function of the reaction time. As time goes on, the H_2 production increases rapidly and tends to be stable after 20 h, exhibiting the sustaining and effective activation of CO by this catalyst (Fig. 4c). The stability of the porous PtPb PNCs-40/ZnO was also investigated by recycling the WGS reaction (Fig. 4d). After ten cycles, the porous PtPb PNCs-40/ZnO largely maintained the original activity for H_2, exhibiting the outstanding stability for WGS, which is crucial for the industrial application. The TEM and HAADF-STEM results reveal that after ten cycles, the porous PtPb PNCs-40/ZnO largely maintained their original structures, further confirming the excellent stability (Fig. S11c, d online). Under the same condition, the commercial Pt/C preserved only 69% initial activity after ten cycles (Fig. S15 online) and experienced severe size change after the stability test (Fig. S16 online). Therefore, the porous PtPb PNCs-40/ZnO exhibits both promising activity and outstanding stability for WGS reaction.

The surface electronic properties of catalyst surfaces are believed as the descriptor for modulating the WGS activity [26]. Hence, we collected XPS of PtPb PNCs/ZnO, porous PtPb PNCs/ZnO, PtPb ONCs/ZnO and porous PtPb ONCs/ZnO and studied the relationship between Pt/Pb ratios, Pt(0)/Pt(II) ratios and WGS activity (Tables S2 and S3 online). Each Pt 4f peak can be deconvoluted into two pairs of doublets (Fig. 5a). According to the deconvolution results, a large proportion of the Pt(0) exists in the porous PtPb PNCs-40/ZnO. The ratio of Pb(0)/Pb(II) in porous PtPb PNCs-40/ZnO (77.8/22.2) is higher than PtPb PNCs/ZnO (43.8/56.2), other porous PtPb PNCs/ZnO (70.3/29.7 for porous PtPb PNCs-30/ZnO and 64.8/35.2 for porous PtPb PNCs-60/ZnO), PtPb ONCs/ZnO

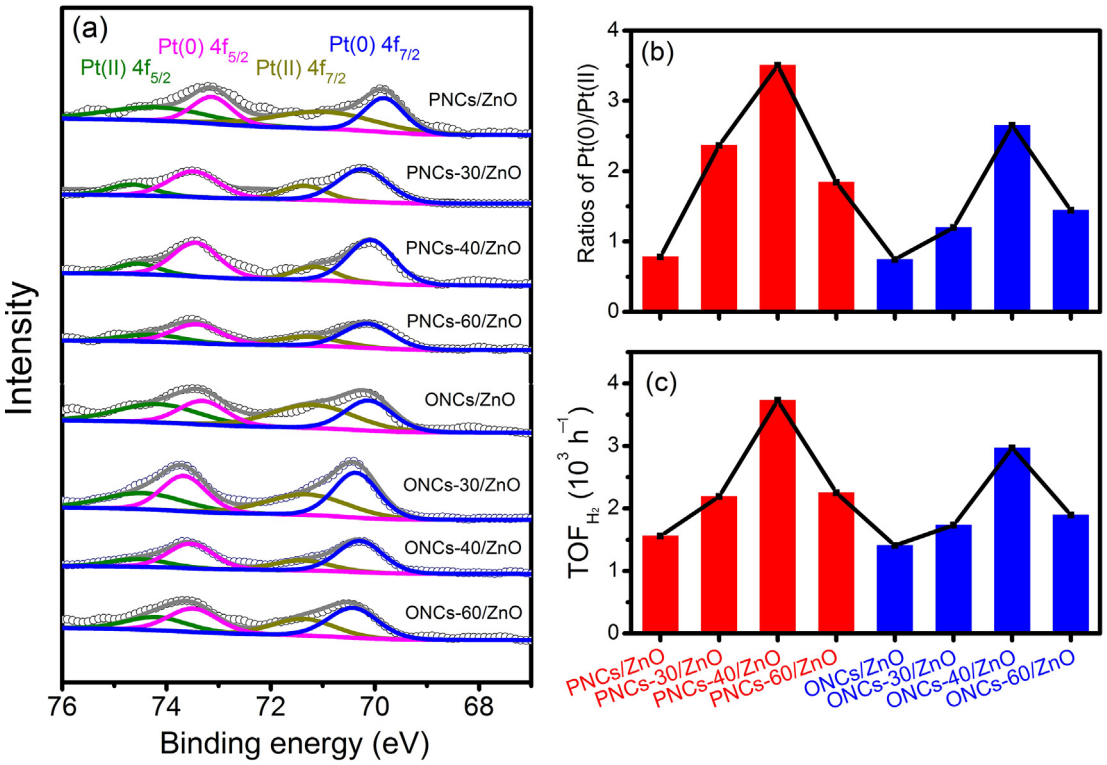

Fig. 5. (Color online) Pt 4f XPS spectra (a), ratios of Pt(0) to Pt(II) (b) and the achieved H_2 TOF values (c) of PtPb PNCs/ZnO, porous PtPb PNCs-30/ZnO, porous PtPb PNCs-40/ZnO, porous PtPb PNCs-60/ZnO, PtPb ONCs/ZnO, porous PtPb ONCs-30/ZnO, porous PtPb ONCs-40/ZnO and porous PtPb ONCs-60/ZnO.

(42.7/57.3) and porous PtPb ONCs/ZnO (54.5/45.5 for porous PtPb ONCs-30/ZnO, 72.6/27.4 for porous PtPb ONCs-40/ZnO and 59.1/40.9 for porous PtPb ONCs-60/ZnO) (Table S2 online). Meanwhile, as shown in Fig. 5b, c, with raising the ratio of Pt(0)/Pt(II), the WGS activity increases, in which the highest content of Pt(0) in porous PtPb PNCs-40/ZnO leads to the highest production of H_2 in WGS.

Except the impact on the ratio of Pt(0)/Pt(II), the ratios of Pt/Pb also affect the CO adsorption ability on Pt surface [26,27], which controls the WGS activity. Therefore, CO stripping experiments were carried out to further investigate the relationship between CO adsorption and Pt/Pb ratios (Fig. 6a and Table S4 (online)). Fig. 6a shows the CO stripping curves of PtPb PNCs/C, porous PtPb PNCs-30/C, porous PtPb PNCs-40/C and porous PtPb PNCs-60/C, where the onset and peak potentials of each catalyst can be clearly observed. As the increase of Pt/Pb ratio, the onset and peak potentials for CO oxidation shift to high position (Fig. 6a), indicating the enhanced CO adsorption strength [28,29]. As a reference, we performed the CO stripping on the commercial 20% Pt/C. Among them, the onset and peak potentials for CO oxidation of the porous PtPb PNCs-60/C with the least content of Pb are similar to that of Pt/C (Fig. 6b), representing a strong CO adsorption strength on the Pt surface. Conversely, the PtPb PNCs/C and the porous PtPb PNCs-30/C with high quantities of Pb show very weak CO adsorption strength, which also reduces the WGS activity. For the porous PtPb PNCs-40/C, the modest onset and peak potentials for CO oxidation represent suitable CO adsorption strength on the Pt surface, shown the enhanced WGS activity. The above results prove that the

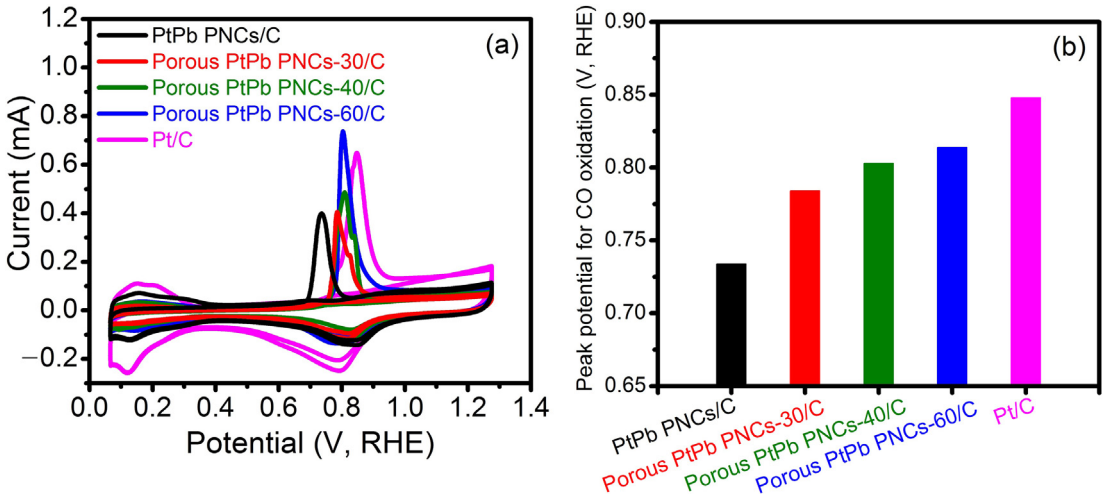

Fig. 6. (Color online) CO stripping voltammograms (a) and the peak potentials for CO oxidation (b) of PtPb PNCs/C, porous PtPb PNCs-30/C, porous PtPb PNCs-40/C, porous PtPb PNCs-60/C and Pt/C.

suitable CO adsorption strength on the Pt surface can enhance the WGS activity. We ascribe the much enhanced performance of the porous PtPb PNCs-40/ZnO for WGS to the most suitable composition of Pt/Pb, nanoporous structure feature, superior geometrical effect, and the optimized interaction between porous PtPb PNCs-40 and ZnO support.

4. Conclusions

To summarize, we have demonstrated porous PtPb PNCs and porous PtPb ONCs with tunable porosity as highly active and stable catalysts towards WGS reaction. The porous degree can be precisely controlled by tuning the acid etching temperature. These porous structures with controllable ratios of Pt/Pb exhibit impressive activity and outstanding durability towards WGS reaction. Among the porous PtPb PNCs and porous PtPb ONCs, the porous PtPb PNCs-40 delivers the highest activity, more than 16.9 times higher than that of the commercial Pt/C. The highest content of Pt(0) and suitable CO adsorption strength on the porous PtPb PNCs-40 ensure the outstanding activity for WGS reaction. In addition, the porous PtPb PNCs-40/ZnO showed excellent stability for WGS over ten cycles without sacrificing the activities. Our finding opens up an exciting strategy towards the rational design of porous Pt-based nanostructures for catalysis and beyond.

Conflict of interest

The authors declare that they have no conflict of interest.

Acknowledgments

This work was supported by the Ministry of Science and Technology of China (2016YFA0204100, 2017YFA0208200), the National Natural Science Foundation of China (21571135), Young Thousand Talented Program, the Natural Science Foundation of Jiangsu Higher Education Institutions (17KJB150032), the Start-up Supports from Soochow University, and the Priority Academic Program Development of Jiangsu Higher Education Institutions (PAPD).

Appendix A. Supplementary data

Supplementary data to this article can be found online at https://doi.org/10.1016/j.scib.2018.11.020.

References

[1] Rodriguez JA, Grinter DC, Liu Z, et al. Ceria-based model catalysts: fundamental studies on the importance of the metal-ceria interface in CO oxidation, the water-gas shift, CO_2 hydrogenation, and methane and alcohol reforming. Chem Soc Rev 2017;46:1824–41.
[2] Ratnasamy C, Wagner JP. Water gas shift catalysis. Catal Rev 2009;51:325–440.
[3] Stere CE, Anderson JA, Chansai S, et al. Non-thermal plasma activation of gold-based catalysts for low-temperature water-gas shift catalysis. Angew Chem Int Ed 2017;56:5579–83.
[4] Sun Y, Hla SS, Duffy GJ, et al. A comparative study of CeO_2-La_2O_3-based Cu catalysts for the production of hydrogen from simulated coal-derived syngas. Appl Catal A Gen 2010;390:201–9.
[5] Kalamaras CM, Dionysiou DD, Efstathiou AM, et al. Mechanistic studies of the water-gas shift reaction over $Pt/Ce_xZr_{1-x}O_2$ catalysts: the effect of Pt particle size and Zr dopant. ACS Catal 2012;2:2729–42.
[6] Bussche KMV, Froment GF. A steady-state kinetic model for methanol synthesis and the water gas shift reaction on a commercial $Cu/ZnO/Al_2O_3$ catalyst. J Catal 1996;161:1–10.
[7] Yang M, Allard LF, Flytzani-Stephanopoulos M, et al. Atomically dispersed Au-$(OH)_x$ species bound on titania catalyze the low-temperature water-gas shift reaction. J Am Chem Soc 2013;135:3768–71.
[8] Fu Q, Saltsburg H, Flytzani-Stephanopoulos M, et al. Active nonmetallic Au and Pt species on ceria-based water-gas shift catalysts. Science 2003;301:935–8.
[9] Rodriguez JA, Ma S, Liu P, et al. Activity of CeO_x and TiO_x nanoparticles grown on Au(1 1 1) in the water-gas shift reaction. Science 2007;318:1757–60.
[10] Qiao BT, Wang AQ, Yang XF, et al. Single-atom catalysis of CO oxidation using Pt_1/FeO_x. Nat Chem 2011;3:634–41.
[11] Shang L, Bian T, Zhang B, et al. Graphene-supported ultrafine metal nanoparticles encapsulated by mesoporous silica: robust catalysts for oxidation and reduction reactions. Angew Chem Int Ed 2014;53:250–4.
[12] Miao DY, Goldbach A, Xu HY, et al. Platinum/apatite water-gas shift catalysts. ACS Catal 2016;6:775–83.
[13] Casado-Rivera E, Volpe DJ, Alden L, et al. Electrocatalytic activity of ordered intermetallic phases for fuel cell applications. J Am Chem Soc 2004;126:4043–9.
[14] Huang YY, Cai JD, Liu MY, et al. Fabrication of a novel PtPbBi/C catalyst for ethanol electro-oxidation in alkaline medium. Electrochim Acta 2012;83:1–6.
[15] Feng YG, Bu LZ, Guo SJ, et al. 3D platinum-lead nanowire networks as highly efficient ethylene glycol oxidation electrocatalysts. Small 2016;12:4464–70.
[16] Gilroy KD, Ruditskiy A, Peng HC, et al. Bimetallic nanocrystals: syntheses, properties, and applications. Chem Rev 2016;116:10414–72.
[17] Wang D, Li Y. Bimetallic nanocrystals: liquid-phase synthesis and catalytic applications. Adv Mater 2011;23:1044–60.
[18] Khan MU, Wang LB, Liu Z, et al. Pt_3Co octapods as superior catalysts of CO_2 hydrogenation. Angew Chem Int Ed 2016;55:9548–52.
[19] Newsome DS. The water-gas shift reaction. Catal Rev Sci Eng 1980;21:275–318.
[20] Zhai YP, Pierre D, Si R, et al. Alkali-stabilized Pt-OH_x species catalyze low-temperature water-gas shift reactions. Science 2010;329:1633–6.
[21] Yang M, Li S, Wang Y, et al. Catalytically active Au-$O(OH)_x$-species stabilized by alkali ions on zeolites and mesoporous oxides. Science 2014;346:1498–501.
[22] Zugic B, Zhang SR, Bell DC, et al. Probing the low-temperature water-gas shift activity of alkali-promoted platinum catalysts stabilized on carbon supports. J Am Chem Soc 2014;136:3238–45.
[23] Laine RM, Rinker RG, Ford PC, et al. Homogeneous catalysis by ruthenium carbonyl in alkaline solution: the water gas shift reaction. J Am Chem Soc 1977;99:252–3.
[24] Yang M, Liu JL, Lee S, et al. A common single-site Pt(II)-$O(OH)_x$-species stabilized by sodium on "active" and "inert" supports catalyzes the water-gas shift reaction. J Am Chem Soc 2015;137:3470–3.
[25] Bunluesin T, Gorte RJ, Graham GW, et al. Studies of the water-gas-shift reaction on ceria-supported Pt, Pd, and Rh: implications for oxygen-storage properties. Appl Catal B Environ 1998;15:107–14.
[26] Yao SY, Zhang X, Zhou W, et al. Atomic-layered Au clusters on α-MoC as catalysts for the low-temperature water-gas shift reaction. Science 2017;357:389–93.
[27] Si R, Flytzani-Stephanopoulos M. Shape and crystal-plane effects of nanoscale ceria on the activity of Au-CeO_2 catalysts for the water-gas shift reaction. Angew Chem Int Ed 2008;47:2884–7.
[28] Xie J, Zhang QH, Gu L, et al. Ruthenium-platinum core-shell nanocatalysts with substantially enhanced activity and durability towards methanol oxidation. Nano Energy 2016;21:247–57.
[29] Sulaiman JE, Zhu SQ, Xing ZL, et al. Pt-Ni octahedra as electrocatalysts for the ethanol electro-oxidation reaction. ACS Catal 2017;7:5134–41.

Bin E obtained his B.S. degree (2015) and M.S. degree (2018) in Materials Science and Engineering from China University of Petroleum, Beijing. Then he worked in CAS&M (Zhangjiagang) New Energy Technology Co., Ltd. as a R&D Engineer. His current research interests focus on the direct methanol fuel cell system integration and fuel efficiency optimization.

Xiaoqing Huang is currently a Professor at College of Chemistry, Chemical Engineering and Materials Science, Soochow University. He obtained his B.S. degree from Southwest Normal University (2005) and Ph.D. degree from Xiamen University (2011). He joined Profs. Yu Huang and Xiangfeng Duan's group as a postdoctoral fellow from 2011 to 2014 at University of California, Los Angeles. His current research interests focus on the design of nanoscale materials for heterogenous catalysis, electrocatalysis, energy conversion and beyond.